

# On the Amari Neural Field

Antonio Franca

June 2023

## 1 Introduction

The primary motivation of neuroscience is to understand how the brain stores and processes information. Neuroscientists have observed several characteristic patterns of neural activity that play a crucial role in how the brain makes this happen. These phenomena reflect the complex and highly coordinated behavior of neural populations. Some of these patterns come in the shape of neural oscillations [3, 10], propagating waves [4, 14], synchronized activity [5], "bursting" behavior [13], chaotic dynamics [8, 15], and ring attractors dynamics [6, 9], among others.

On the other hand, applied mathematics provides us with sophisticated tools and methodologies, such as dynamical systems theory, that can be used to model and understand complex systems. Dynamical systems theory, in particular, has proven to be a potent tool for understanding the temporal evolution and behavior of neural systems. This intersection of neuroscience and applied mathematics gives rise to the field of mathematical neuroscience. The goal of mathematical neuroscience is to employ mathematical models and techniques to understand the principles governing brain function, providing us with a systematic way to translate biological observations into a theoretical framework.

In this context, the study of neural fields is of particular interest. Neural field equations (NFEs) are mathematical models that describe the spatiotemporal dynamics of neural populations in the brain assuming the cortical tissue is a continuous medium. Several types of NFEs such as Wilson-Cowan Model [16], FitzHugh-Nagumo Model [7], or Nunez Model [11] have been developed, each designed to capture different aspects of neural dynamics. However, along this exploration, we will consider one specific NFE type for some of its desirable properties, concretely, the one introduced by Amari [1].

The Amari neural field model describes the evolution of neuron firing rates in a continuous

field of neurons. The basic form of the Amari neural field model is as follows

$$\begin{aligned}\partial_t u(x, t) &= -u(x, t) + \int_{\Omega} \omega(x, y) f(u(y, t)) dy + I(x, t) \\ u(x, 0) &= v(x)\end{aligned}\tag{1}$$

with  $(x, t) \in \Omega \times \mathbb{R}_{>0}$ . Here,  $\Omega$  represents the cortex, and  $v(x)$  is an initial profile function. The notation  $u(x, t)$  represents the mean firing rate of the neurons at position  $x$  at time  $t$ . The integral term represents the interaction between different neurons, where  $\omega(x, y)$  is a synaptic connectivity kernel describing the influence of the firing rate at position  $y$  on the firing rate at position  $x$ . The function  $f(u)$  is a nonlinearity function, typically representing a threshold effect: neurons do not fire unless their input is above a certain threshold. Finally,  $I(x, t)$  is an external input applied to the neurons at position  $x$  at time  $t$ . Observe that this set-up can be cast as a Cauchy problem on a Banach space.

Throughout this paper, we will introduce additional assumptions for the model. These assumptions will balance the need for mathematical simplicity with the requirement for the model to correspond reasonably well to reality. This paper is structured in the following manner: Section 2 is dedicated to an exploration and theoretical analysis of the Amari Neural Field Equation. In Section 3, we implement numerical methods to model a neural field equation, and use it to find confirmation of the theoretical results drawn in the previous section. Lastly, we will try to reproduce some of the experimental outcomes observed in a relevant neuroscience paper.

## 2 Analytical Exploration

Consider the Amari neural field model, with same notation as in Equation 1, under the following hypotheses

- The cortex  $\Omega$  is an interval of the real line  $D = [-L, L] \subset \mathbb{R}$ , with  $L = \pi$ .
- The homogeneous synaptic kernel is given by  $\omega(z) = (1 - |z|)e^{-|z|}$ .
- The firing rate is a sigmoidal function

$$f(u) = \frac{1}{1 + \exp(-\mu u)}, \text{ for } \mu = 10$$

- The external stimulus is null,  $I(x, t) \equiv 0$ .

Let us briefly explain the motivation of the assumptions. We choose the cortical tissue to be portrayed as a subspace of  $\mathbb{R}$  for mathematical convenience. However, this assumption still makes some correspondence to reality. We select  $L = \pi$  with the intention of using the position  $x$  as a measure of angular orientation if we consider the brain as the topological  $S^1$ . We obtain this via reparametrization  $\phi : [-\pi, \pi] \rightarrow S^1$  using the mapping  $\phi(x) = (\cos(x), \sin(x))$  which can easily be linked to a point in  $S^1$ .

We assume the synaptic kernel to be  $w(z) = (1 - |z|) e^{-|z|}$ , as it satisfies some desirable properties. In particular,  $w(z)$  is symmetric and portrays the idea of strong connections for nearby neurons, pronounced inhibition at intermediate distances, and minor inhibitory connections for neurons located at greater distances. This synaptic kernel corresponds to strength connection in reality for neurons within small chunks of the brain.

The choice of the sigmoid function for the nonlinearity is motivated for several reasons. It has been observed that neurons typically have a certain threshold of activation, below which they do not fire and above which they fire at a constant rate. The sigmoid function, with its S-shaped curve, provides a good mathematical model of this behavior. Furthermore, this function is smooth, non-linear (which is crucial for learning as proven in deep neural networks literature) and outputs a value between 0 and 1.

For the last assumption, we choose the external input function  $I(x, t)$  to be 0 for mathematical simplicity. Realistically, there exist an infinite array of diverse situations, and defining  $I(x, t)$  for each can prove to be incredibly complex. Given these complexities, we choose to examine the most straightforward situation, one in which the agent is entirely isolated - devoid of any external stimuli like noise, vision (in darkness), and so forth.

## 2.1 Homogeneous Equilibrium Solutions

Once we introduced all the assumptions and, inspired by the principles of dynamical systems theory, we will start the analytical study of Equation 1 as an average aspiring mathematician would proceed, that is, by examining the homogeneous equilibrium of the model. To find these equilibria, we set  $\partial_t u(\theta, t) = 0$ , which yields

$$u(x, t) = \int_{\mathbb{R}} \omega(x - y) f(u(y, t)) dy.$$

Since we are just looking for a homogeneous steady-state, we get rid of the dependence of time and space, so that our equation becomes

$$u = \int_{\mathbb{R}} \omega(y) f(u) dy = f(u) \cdot W_0.$$

where  $W_0 = \int_{\mathbb{R}} \omega(y) dy$ . Without loss of generality, we set  $W_0 = 1$  and get the iterated map

$$u_{k+1} = f(u_k).$$

which will lead us to the fixed-point solution  $u^* = f(u^*)$ . Observe then that the solution of the fixed point equation is given by the intersection between the sigmoidal function  $f(u)$  and the straight linear function  $u$ . Thus, depending on the parameters, this fixed point equation raises three distinct cases of interest: a state with one equilibrium close to zero, a state with three distinct equilibria, and a state with one equilibrium close to one. We illustrate these three scenarios in Figure 1

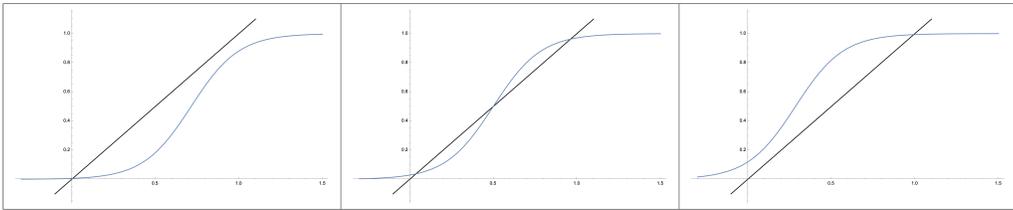


Figure 1: Three cases for the homogeneous equilibrium points with  $b = -5$ ,  $b = -3.5$  and  $b = -2$ .

To assess the stability of an equilibrium point  $u^*$  we study the Taylor series around this equilibrium point  $u^*$ ,

$$f(u) = f(u^*) + df(u^*)(u - u^*) + h.o.t. = u^* + df(u^*)(u - u^*) + h.o.t.$$

where we used that  $u^* = f(u^*)$  by definition. By relocating  $u^*$  to the left side, taking absolute values, and disregarding the terms of higher order, we are led to the inequality  $|f(u) - u^*| \leq |df(u^*)||u - u^*|$ . In terms of the previously established iterated map, we observe that

$$|u_{k+1} - u^*| \leq |df(u^*)||u_k - u^*|.$$

This means that if  $|df(u^*)|$  is less than 1, we have a contraction mapping, which indicates that the equilibrium point  $u^*$  is stable, and vice versa for  $|df(u^*)|$  bigger than 1. Therefore, we just have to take the derivative of  $f$  with respect to  $u$  to study stability.

For this purpose, we can easily look at the slope of the sigmoid function at the intersection points (fixed points) with the diagonal in Figure 1. The diagonal line serves as a reference with a slope of 1. If the sigmoid function exhibits a shallower gradient at that intersection point, the fixed point is considered stable. Conversely, if the gradient is steeper, the fixed point is deemed unstable. We conclude that homogeneous equilibrium points with voltages

close to either 0 or 1 tend to be stable points, while homogeneous equilibrium points with medium voltage values are unstable.

The primary takeaway from this subsection is the understanding that the homogeneous equilibrium points of the Amari model, under our stated assumptions, are dependent on the parameters of the sigmoid function. In other words, the firing rate will determine the homogeneous equilibrium points and the degree of network activity.

## 2.2 Non-Homogeneous Stationary Solutions.

Following our initial analytical investigation and the preliminary conclusions drawn, we now progress to the next logical stage: identifying non-homogeneous equilibria. For mathematical convenience, in this subsection, we will change one of the previously taken assumptions. We will assume the firing rate is of Heaviside type,  $f(u) = H(u)$ , since it resembles some of the desirable properties we mentioned on the sigmoid, but will behave more conveniently for deriving analytical results.

We wonder about the existence of stationary localised steady states of the neural field model which we will denote by  $U(x)$ . In this hypothetical solution, the system reaches an equilibrium with respect to time  $t$ , and therefore  $U(x)$  satisfies

$$\begin{aligned} 0 &= -U(x) + \int_{\mathbb{R}} \omega(x-y) H(U(y) - h) dy \\ \rightarrow U(x) &= \int_{\mathbb{R}} \omega(x-y) H(U(y) - h) dy. \end{aligned} \tag{2}$$

Since we aim to find  $U(x)$  with a nontrivial spatial profile, we assume that  $U(x) \geq h$  for all  $x \in [x_1, x_2]$  for some  $x_1, x_2$ , and where  $h = U(x_1) = U(x_2)$ .

Note that if this does not hold, the integral of the Equation 2 equates to 0, and  $U(x) = 0$  is the trivial solution. Using this conceptual observation, and following the nature of the Heaviside function we see that

$$U(x) = \int_{x_1}^{x_2} \omega(x-y) dy. \tag{3}$$

Using this result, we aim to find an explicit solution for the stationary localised steady states. First, we prove a general statement which holds for our chosen synaptic kernel, and which will be utilized in the derivation of an explicit formula for the bump solution.

**Lemma 1.** Consider the cortical tissue as a subspace of  $\mathbb{R}$ , and assume the synaptic kernel to be  $w(z) = (1 - |z|) e^{-|z|}$ . Then,

$$\int_a^x \omega(x - y) dy = (x - a)e^{-|x-a|}.$$

*Proof.* Without loss of generality, let  $a < x$  for some generic  $a, x \in \mathbb{R}$ . We see that

$$\begin{aligned} \int_a^x \omega(x - y) dy &= \int_a^x w(y - x) dy = \int_{a-x}^0 w(y) dy \\ &= \int_{a-x}^0 (1 - |y|) e^{-|y|} dy = \int_{a-x}^0 (1 + y) e^y dy \\ &= \int_{a-x}^0 e^y + \int_{a-x}^0 y e^y = \int_{a-x}^0 e^y + y e^y \Big|_{a-x}^0 - \int_{a-x}^0 e^y \\ &= -(a - x)e^{a-x} = (x - a)e^{-|x-a|}. \end{aligned}$$

□

Along this proof, we use the fact that the synaptic kernel is a symmetric function in the first equality, and the fourth equality comes from the fact that we are integrating over negative values of  $y$ , since  $a < x$ . We can now use this result to obtain a bump solution for the neural field model. Substituting our kernel function into Equation 3 and splitting it for an arbitrary  $x \in [x_1, x_2]$  yields

$$\begin{aligned} U(x) &= \int_{x_1}^{x_2} \omega(x - y) dy = \int_{x_1}^x \omega(x - y) dy + \int_x^{x_2} \omega(x - y) dy \\ &= (x - x_1)e^{-|x-x_1|} + (x_2 - x)e^{-|x_2-x|} \\ &= \operatorname{sgn}(x - x_1) \cdot |x - x_1| \cdot e^{-|x-x_1|} + \operatorname{sgn}(x_2 - x) \cdot |x_2 - x| \cdot e^{-|x_2-x|}. \end{aligned}$$

We conclude with an explicit bump solution to the neural field model, namely

$$U(x) = \operatorname{sgn}(x - x_1)\psi(|x - x_1|) + \operatorname{sgn}(x_2 - x)\psi(|x_2 - x|), \quad (4)$$

where  $\psi(x) = xe^{-x}$ . Once obtained the explicit expression for the bump solution  $U(x)$ , we want to get some information on what this function looks like and reach some conclusions about how nicely does it behave. First, we wonder about the long-term behaviour of this function. By taking the limit, we easily see that

$$\lim_{x \rightarrow \pm\infty} U(x) = \lim_{x \rightarrow \pm\infty} (x - x_1)e^{-|x-x_1|} + (x_2 - x)e^{-|x_2-x|} = 0.$$

This is because the exponential term approaches 0 for both  $\pm\infty$  at a faster rate than the linear factor tends towards  $\pm\infty$ . We also want to check whether this function satisfies some smoothness. In particular, we make the following claim.

**Lemma 2.** *The function  $U(x) = \text{sgn}(x - x_1)\psi(|x - x_1|) + \text{sgn}(x_2 - x)\psi(|x_2 - x|)$  satisfies  $U(x) \in C^1(\mathbb{R})$ .*

*Proof.* First, we note that

$$\begin{aligned} U(x) &= \text{sgn}(x - x_1)\psi(|x - x_1|) + \text{sgn}(x_2 - x)\psi(|x_2 - x|) \\ &= (x - x_1)e^{-|x-x_1|} + (x_2 - x)e^{-|x_2-x|}. \end{aligned}$$

It is trivial to see that the function  $f(x) \equiv (x - x_1)e^{-|x-x_1|}$  is continuously differentiable for all  $x$  different from  $x_1$ , and the function  $g(x) \equiv (x_2 - x)e^{-|x_2-x|}$  is continuously differentiable for all  $x$  different from  $x_2$ . We check differentiability of the first function  $f(x)$  at  $x_1$  by looking at the limit definition of the derivative at  $x_1$ . In particular, we see that

$$\frac{d}{dx}f(x_1) = \lim_{h \rightarrow 0} \frac{f(x_1 + h) - f(x_1)}{h} = \lim_{h \rightarrow 0} \frac{he^{|h|}}{h} = \lim_{h \rightarrow 0} e^{|h|} = 1 < \infty.$$

Analogously for  $g(x)$  at  $x_2$ ,

$$\frac{d}{dx}g(x_2) = \lim_{h \rightarrow 0} \frac{g(x_2 + h) - g(x_2)}{h} = \lim_{h \rightarrow 0} \frac{-he^{|h|}}{h} = \lim_{h \rightarrow 0} -e^{|h|} = -1 < \infty.$$

We see that both  $f$  and  $g$  are continuously differentiable for all  $x$ , and therefore  $U(x)$  is continuously differentiable for all  $x$ . □

As a final verification, we opt to plot this function for  $x_1 = 0$  and  $x_2 = 1$ , to gain a clearer understanding on the appearance of the solution  $U(x) = x e^{-|x|} + (1 - x) e^{-|1-x|}$ .

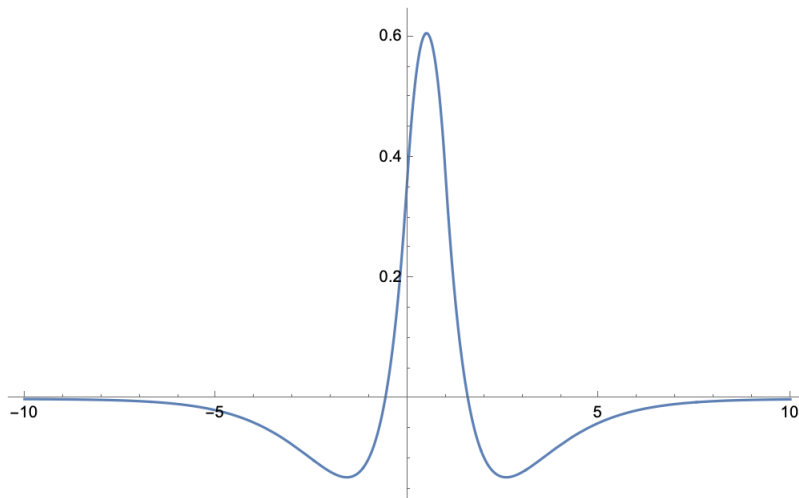


Figure 2: Plot of  $U(x)$  for the initial conditions  $x_1 = 0$  and  $x_2 = 1$ .

Notice how the spike is succeeded by the recovery phase, and how the signal vanishes in the long-term. This conclusion makes us think of the non-homogeneous solution profile as

somewhat of a bump, as the solution rises above the baseline level of neural activity, forms a "bump" or peak, and then returns to the baseline. Furthermore, we now know that this solution is smooth, bell-shaped vanishing at infinity, and represents a concentrated region of high neural activity in a background of lower activity.

### 2.3 Bifurcation Analysis

We finish the section with some bifurcation theory, where we study how the choice of  $h$  will affect the bump solution. Following our previous results, we observed that the theoretical bump solution depends on the values  $x_1$  and  $x_2$ , as in Equation 4. Let  $x_2 - x_1 = \Delta$  as a measure of the bump width. Recall that, by construction,  $h = U(x_1)$ . Thus, we see that

$$\begin{aligned} h = U(x_1) &= \int_{x_1}^{x_2} \omega(x_1 - y) dy = - \int_{x_2}^{x_1} \omega(x_1 - y) dy = -(x_1 - x_2)e^{-|x_1 - x_2|} \\ &= (x_2 - x_1)e^{-(x_2 - x_1)} = \Delta e^{-\Delta} = \psi(\Delta), \end{aligned}$$

where  $h$  is the threshold parameter. Now, we use  $h = \psi(\Delta)$  to plot in Figure 3 a bifurcation diagram for bump solutions, in the parameter  $h$  with solution measure  $\Delta$ .

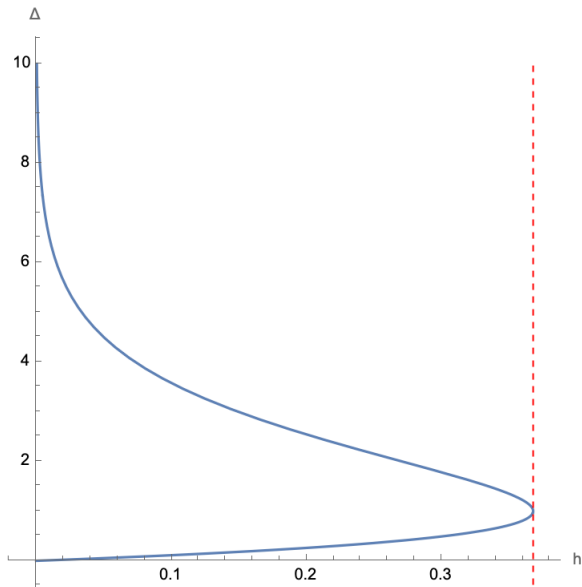


Figure 3: Bifurcation Diagram for parameter  $h$ , and red vertical line  $h = 1/e$ .

The bifurcation diagram shows the dependence of bump solutions, as defined in Equation 4, on the parameter  $h$ . Specifically, for  $h < 1/e$ , two distinct types of width  $\Delta$  are found to be compatible with the existence of a theoretical bump solution. When  $h$  equals  $1/e$ , there is precisely one unique bump solution, and, the scenario for  $h > 1/e$  yields no such solutions.

We recognise here a saddle-node bifurcation type, where varying the parameter  $h$  makes the disappearance of two equilibria in the system. In particular, this happens for the value  $h = 1/e$ , which is plotted as a vertical line in Figure 3.

### 3 Numerical Simulation

#### 3.1 Finite-Elements Collocation Method

After doing the analytical exploration, we have come to the point where continuing without the numerical methods becomes unfeasible. The latter will enable us to perform experiments and, ideally, provide meaningful insights into the Amari model. As shown in the recent work of Avitabile [2], projection methods can be effectively used for solving neural field equations. Due to time constraints, we rely on the authenticity of Avitabile’s work and our consistent implementation of the Finite-Elements Collocation Method, employing it without providing comments on numerical convergence.

Consider a neural field model of the Amari type, as in Equation 1, under the assumptions stated at the beginning of Section 2. As we said, we aim to solve it by numerically approximating Equation 1. For that purpose, we decide to implement the Finite-Elements Collocation Method. We start by dividing the domain  $\Omega = [-L, L]$  of the problem into a finite number of  $n$  evenly-spaced elements for some  $n \in \mathbb{N}$ . This division yields a set of collocation points  $\{x_i \text{ s.t. } x_i = -L + \frac{2}{n}i; \forall i \in \{1, 2, \dots, n\}\}$ , which are evenly separated by a  $\Delta x = \frac{2L}{n-1}$  distance. Since these collocation points are part of the domain, Equation 1 still holds on them, so that

$$\partial_t u(x_i, t) = -u(x_i, t) + \int_{-\pi}^{\pi} \omega(x_i, y) f(u(y, t)) dy + I(x_i, t)$$

for  $i \in \{1, 2, \dots, n\}$ . Note that the main difficulty in this differential equation is dealing with the integral. Thus, the next step is using the collocation points to approximate the integral by a sum, and with this we obtain a completely discretized system. In particular, we use the composite trapezoidal rule to make this approximation <sup>1</sup>. As shown in [12], this trapezoidal formula is second-order accurate with respect to  $\Delta x$ , which means that the error in the approximation decreases quadratically as the step size decreases.

This approximation enables us then to choose a set of basis functions to approximate the

---

<sup>1</sup>The composite trapezoidal rule uses piecewise-linear interpolations of the function we want to integrate at the aforementioned collocation points.

solution within each element, so that Equation 1 becomes

$$\dot{u}_i(t) \approx -u_i(t) + \sum_{j=0}^n \omega(x_i, x_j) f(u_j(t)) \rho_j + I_i(t), \quad \text{with } t \in \mathbb{R}_{>0}$$

$$u(x_i, 0) = v(x_i)$$

where  $\rho_j = \Delta x/2$  for  $j \in \{0, n\}$ , and  $\rho_j = \Delta x$  otherwise. Note we used the notation  $u_i(t) = u(x_i, t)$ ,  $I_i(t) = I(x_i, t)$ , and the dot notation for the derivative with respect to time, that is, the only independent variable in the discretized system. This discretized system can be expressed in a vectorial notation so that

$$\frac{d}{dt} U(t) \approx -U(t) + M \cdot F(U(t)) + I(t), \quad \text{with } t \in \mathbb{R}_{>0}$$

$$U(0) = V$$
(5)

where  $M$  is a matrix whose entry  $M[i, j] = \omega(x_i, x_j) \rho_j$ . Note that Equation 5 is nothing by a large system of linear differential equations, which can be solved using various numerical techniques. In practice, we will use `ode45()` in MATLAB to solve this system of equations. We provide the code implementation function of this algorithm in Listing 1.

### 3.2 Theoretical Validation using Numerics

Now that we have a mechanism for simulating the Amari equation, our goal is to generate numerical evidence that corroborates the theory we previously formulated in the analytical section. First, we briefly check that the Amari model supports two types of stationary solutions, namely a homogeneous equilibrium solution, and a stationary bump solution (non-homogeneous).

For simplicity, we simulate a straightforward stationary solution,  $U(x) \equiv 0$ , in the case of homogeneity. This was achieved by setting the initial profile function to a constant value of 0. However, in our attempt to simulate this homogeneous, trivial solution of  $U(x) \equiv 0$ , instead of a consistent flat state throughout the entire time period, we observed an extremely small fluctuation in behaviour. To solve this problem, we opted to use the Heaviside firing rate function instead of the sigmoid function. Our choice is justified by the fact that the Heaviside function essentially becomes the sigmoid function as  $\mu$  approaches infinity.

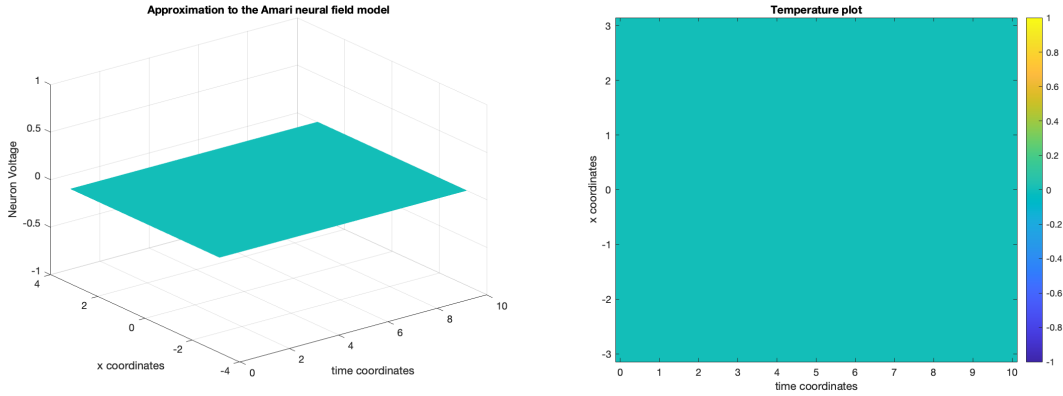


Figure 4: Trivial stationary solution  $U(x) \equiv 0$  with code in Listings 2.

In our study of the non-homogeneous steady state, we not only confirmed its existence, but we also verified that one of the observable non-homogeneous bump solutions aligns with the one we derived in the analytical section, namely

$$U(x) = \text{sgn}(x - x_1)\psi(|x - x_1|) + \text{sgn}(x_2 - x)\psi(|x_2 - x|),$$

where  $\psi(x) = xe^{-x}$ . To get this, we simply set the initial profile to the theoretically predicted stable bump solution and affirmed that it indeed produced a bump solution.

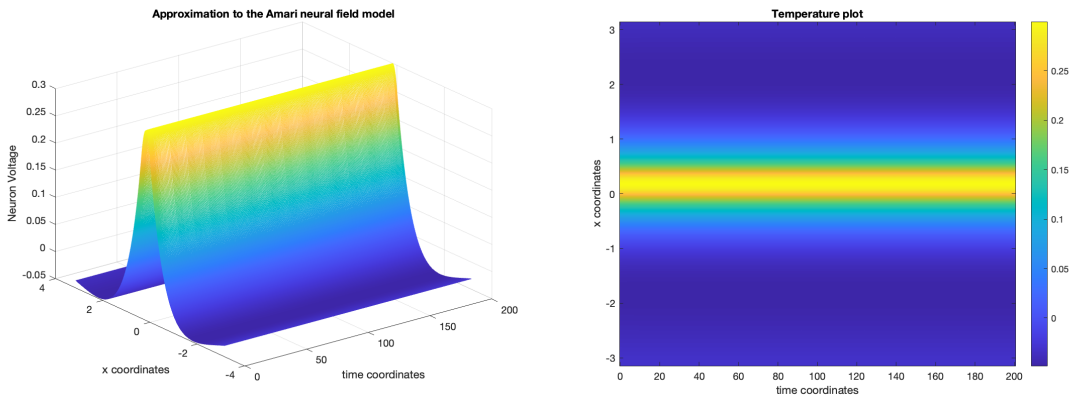


Figure 5: Theoretical Stationary Bump Solution  $U(x)$  with code in Listings 3.

One observation we made is that this secondary approach yields results only when the Heaviside type is utilized as the firing rate function. Conversely, when the sigmoid function is used, we generally obtain a vanishing solution or a bump solution that differs from the one predicted theoretically. This corresponds to the assumption we introduced to achieve this bump solution in the analytical section.

Finally, we also confirmed the theoretical outcomes derived from our bifurcation analysis. The primary theoretical understanding is that for a choice of  $h < 1/e$ , two distinct bump solutions exist; for  $h = 1/e$ , there is a single bump solution, and for  $h > 1/e$ , there are no bump solutions. For a more visual understanding, we've included some of these scenarios in Figure 9 in the Appendix.

Specifically, we exemplify the existence of two unique bump solutions in cases where  $h = 0.25$ , which is representative of conditions where  $h < 1/e$ . Additionally, we showcase the plot corresponding to the scenario where  $h = 1/e$ , leading to  $\Delta = 1$ . Lastly, we encourage the reader to explore what happens when  $h > 1/e$  using the provided code in the Appendix. Based on our findings, we predict that the result will be a vanishing system.

To validate the results of our bifurcation analysis, we carried out simulations for various values of  $h$  and assessed the resultant width  $\Delta$  of the formed bump. The observed results, illustrated in Figure 6, demonstrate a correlation between the experimentally obtained widths and those predicted theoretically, thereby reinforcing our prior theoretical assertions.

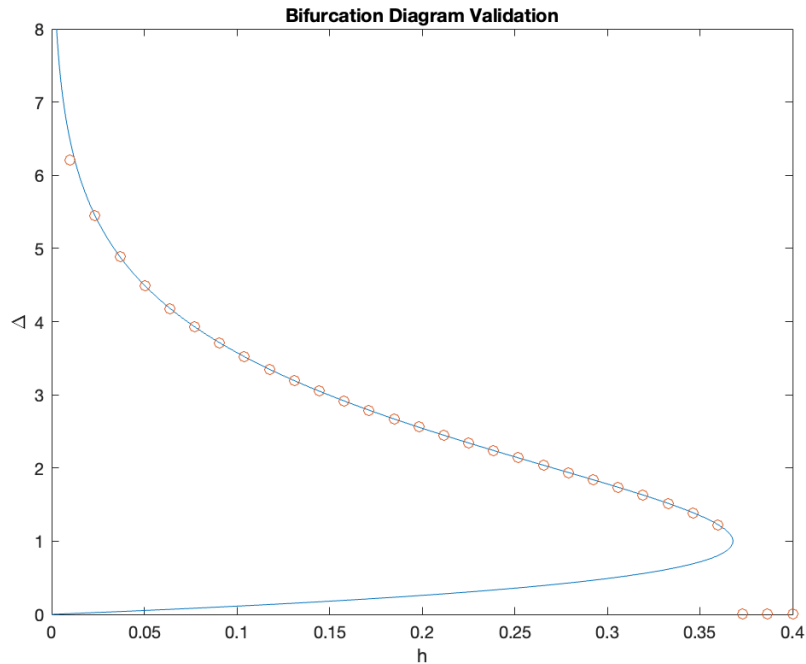


Figure 6: Bifurcation Diagram Validation with code in Listings 4.

Note, for  $h > 1/e$ , the `psi` function in the code does not yield any roots and returns NaN. This provides an explanation for the positioning of those points located on the x-axis to the right of  $1/e$ .

### 3.3 Heading Representation of the flies

Finally, we turn on the stimulus function and try to replicate some of the experimental results obtained in the *Kim et al* paper [9]. This study reported that a population of neurons, called E-PG neurons, in the *Drosophila melanogaster* ellipsoid body (EB) appears to use bump-like neural activity dynamics to represent the animal’s heading in visual environments and in darkness.

The researchers first determined whether the E-PG population activity bump tracks the fly’s heading direction relative to its visual surroundings during tethered flight. As with walking flies, neural population activity during flight was organized into a single bump, where they observed that the visual scene contained a complex pattern (Fig.1G in [9]). However, unlike in walking, the activity bump seldom tracked the fly’s motor actions in darkness (Fig.1H in [9]).

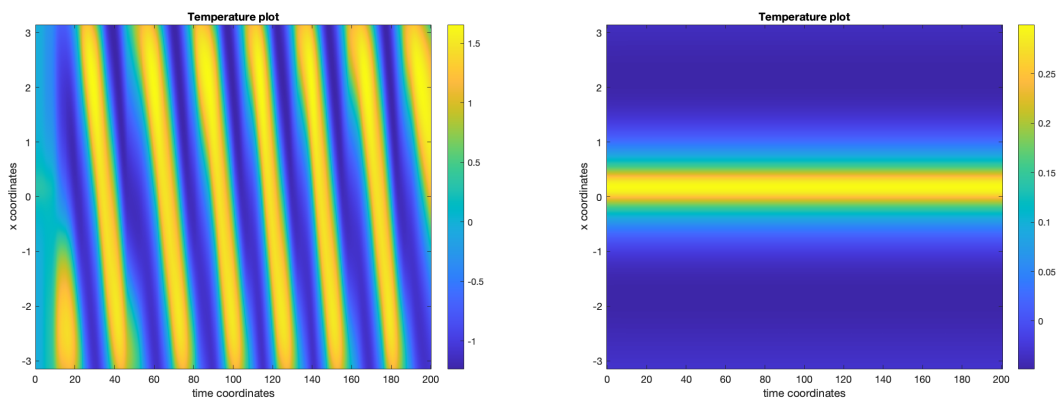


Figure 7: Left replicates Fig.1G. Right replicates Fig.1H. with code in Listings 5

We have reproduced these two empirical observations in Figure 7. To recreate the complex pattern, as shown in Figure 1G in the original paper, we employed a sinusoidal function (refer to the code in the appendix). Conversely, for the bump observed during the animal’s flight in darkness, as depicted in Figure 1H in the original paper, we utilized a constant external input function with a value of 0, which naturally corresponds to the no-visual input function in reality. Note that our selection of the domain  $[-\pi, \pi]$  is justified analogously to the discretization in the Regions of Interest (ROIs) as per the original paper. This justification is grounded in the parametrization  $\phi$  that we introduced at the beginning of the Analytical section.

Secondly, the researchers probed the network’s response to more artificial conditions, such

as abrupt visual stimulus shifts. Depending on the distance of the shift, they observed the E-PG bump either “flowed” continuously (Fig.4A in [9]) or “jumped” to the new location (Fig.4B in [9]).

We have successfully replicated the first case scenario. In order to achieve this, we utilized an artificially constructed bump function as the external input (refer to the appendix for the code), enabling us to reorient the naturally occurring bump to a location of our choosing. Despite our efforts, we encountered difficulties implementing the “jump” discontinuity, pointing to this scenario as a potential constraint of the Amari model. Nevertheless, we refrain from drawing definitive conclusions on this matter, since it remains uncertain whether this is an inherent limitation of the model, or merely a reflection of our limited creativity to come up with external input functions.

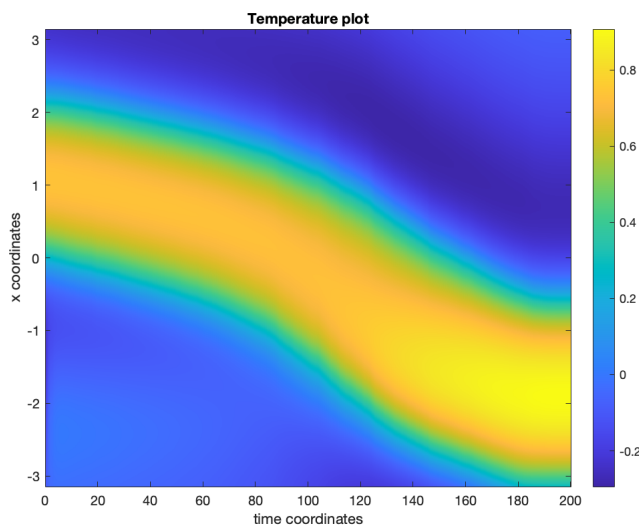


Figure 8: Continuous Flow Change replication with code in Listings 6.

We conclude this report with our brief reproductions of the experiments. Our work affirms that the Amari model proves to be a potent tool in understanding and simulating certain observed experimental results related to the brain function. More specifically, this model provides pivotal insights into bump solutions. For example, in the course of replicating brain dynamics induced by heading representation, it was observed that this Amari model maintained the uniqueness of the bump solution, which is fundamental given that an animal can face only one direction at a given time, and demonstrated persistence, a key attribute enabling an animal to maintain its bearings even in darkness.

## 4 Appendix

Listing 1: Finite-Elements Collocation Method function:

```
function [x, t, uHist] = finiteElementsCollocationMethod(h, external_input, initial_profile )

    %% Create the spatial grid
    nx = 2000;
    L = pi;
    x = linspace(-L,L,nx)';
    delta_x = (2.0*L)/(nx-1);

    %% Synaptic kernel matrix
    omega = @(x,y) (1.0 - abs(x-y)).*exp(-abs(x-y));
    rho = delta_x*[0.5; ones(nx-2,1); 0.5];

    W = zeros(nx,nx);
    for i = 1:nx
        for j = 1:nx
            W(i,j) = omega(x(i),x(j))*rho(j);
        end
    end

    %% Firing Rate Function
    mu = 50; % condition: mu >> 1, sigmoid to Heaviside as mu --> inf;
    sigmoid = @(u) 1.0./(1.0+exp(-mu*(u-h)));
    Heaviside = @(u) (u-h >= 0);

    %% RHS Function
    N = @(t,u) -u + W*sigmoid(u) + external_input(x,t);

    %% Run Dynamics
    tspan = [0, 200];
    [t, uHist] = ode45(N,tspan,initial_profile(x));
end
```

Listing 2: Homogeneous Trivial Solution code (use Heaviside type in the FECM function):

```

h = 0.25;
constant = @(x, t) 0.0;
initial_profile = @(x) 0.0*x;

[x, t, uHist] = finiteElementsCollocationMethod(h, constant, initial_profile );

figure;
mesh(t,x,uHist')
title('Approximation_to_the_Amari_neural_field_model')
xlabel('time_coordinates')
ylabel('x_coordinates')
zlabel('Neuron_Voltage')

figure;
imagesc(t,x,uHist');
colorbar;
title('Temperature_plot');
xlabel('time_coordinates');
ylabel('x_coordinates');
axis xy;

```

Listing 3: Non-Homogeneous Bump Solution code (use Heaviside type in the FECM function):

```

h = 0.25;
constant = @(x,t) 0.0;

psi = @(x) x.*exp(-x);
x1 = 0.0;
x2 = x1 + fzero(@(x) x.*exp(-x) - h, 1);
initial_profile = @(x) sign(x-x1).*psi(abs(x-x1)) + sign(x2-x).*psi(abs(x2-x));

[x, t, uHist] = finiteElementsCollocationMethod(h, constant, initial_profile );

figure;
mesh(t,x,uHist')
title('Approximation_to_the_Amari_neural_field_model')
xlabel('time_coordinates')
ylabel('x_coordinates')
zlabel('Neuron_Voltage')

figure;
imagesc(t,x,uHist');
colorbar;
title('Temperature_plot');
xlabel('time_coordinates');
ylabel('x_coordinates');
axis xy;

```

Listing 4: Bifurcation Analysis Validation code:

```

%% Cleaning
clear, clc;

%% External Input Function
external_input = @(x, t) 0.0;

%% Bifurcation Analysis Validation
h_min = 0.01;
h_max = 0.4;
nh = 30;

h_values = linspace(h_min, h_max, nh);
delta_values = zeros(size(h_values));

for i = 1:length(h_values)

    h = h_values(i);

    % initial Profile Function for this h
    psi = @(x) x.*exp(-x);
    x1 = 0.0;
    x2 = x1 + fzero(@(x) x.*exp(-x) - h, 2.5);

    initial_profile = @(x) sign(x-x1).*psi(abs(x-x1)) + sign(x2-x).*psi(abs(x2-x));

    [x, t, uHist] = finiteElementsCollocationMethod(h, external_input, initial_profile );

    uFinal = uHist(end,:);

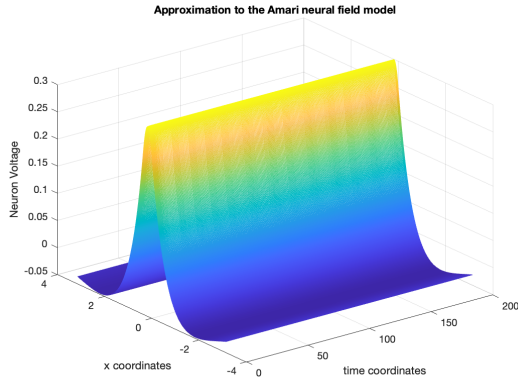
    % measure delta
    [~, idx] = mink(abs(uFinal - h), 2);
    delta_values(i) = x(max(idx)) - x(min(idx));
end

%% Theoretical Bifurcation Diagram
delta_min = 0;
delta_max = 8;
ndelta = 200;

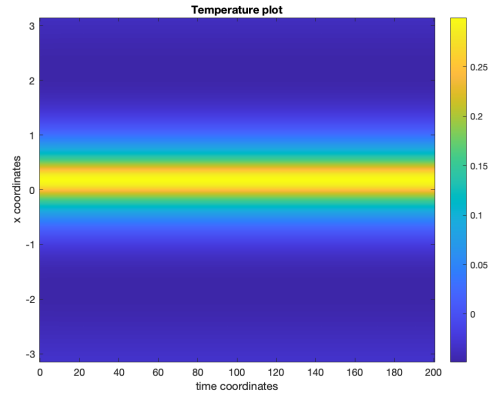
psi = @(x) x.*exp(-x);
delta = linspace(delta_min, delta_max, ndelta);

figure;
plot(psi(delta), delta);
hold on;
plot(h_values, delta_values, 'o')
hold off;
title('Bifurcation_Diagram_Validation');
xlabel('h');
ylabel('\Delta');

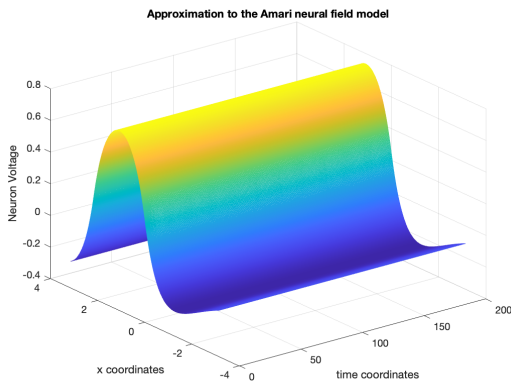
```



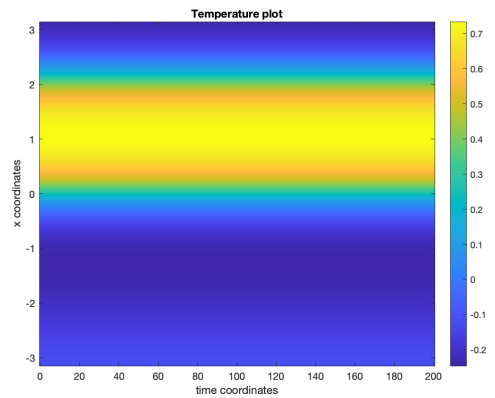
(a) First Bump solution for  $h = 0.25$ .



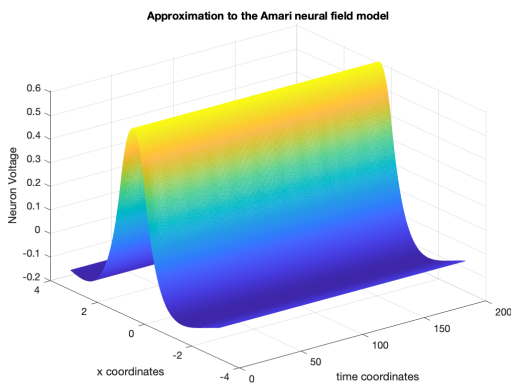
(b) Temp. for the first profile.



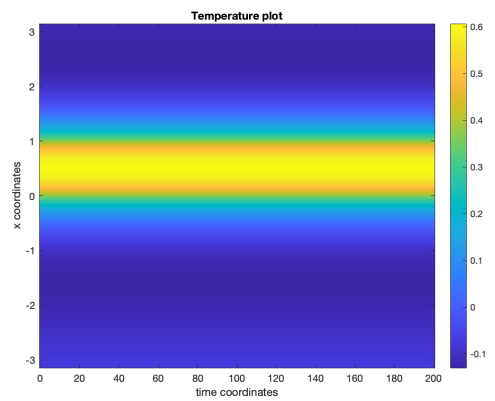
(c) Second Bump solution for  $h = 0.25$ .



(d) Temp. for the second profile.



(e) Unique Bump solution for  $h = 1/e$ .



(f) Temperature for  $h = 1/e$ .

Figure 9: Visualization of the Bifurcation Analysis.

Listing 5: Flying Observation Replication Code (use Heaviside type in the FECM function):

```

h = 0.25;

gAm = 0.2;
mu = -2; % position
sigma = 0.9; % width
external_input = @(x, t) gAm * exp(-(x - mu).^2 / (2 * sigma^2));

psi = @(x) x.*exp(-x);
x1 = 0.0;
x2 = x1 + fzero(@(x) x.*exp(-x) - h, 2.5);

initial_profile = @(x) sign(x-x1).*psi(abs(x-x1)) + sign(x2-x).*psi(abs(x2-x));

%% Run Dynamics
[x, t, uHist] = finiteElementsCollocationMethod(h, external_input, initial_profile );

figure;
imagesc(t,x,uHist');
colorbar;
title('Temperature_plot');
xlabel('time_coordinates');
ylabel('x_coordinates');
axis xy;

```

Listing 6: Continuous Flow Change replication Code:

```

h = 0.25;

gAm = 0.2;
mu = -2; % position
sigma = 0.9; % width
external_input = @(x, t) gAm * exp(-(x - mu).^2 / (2 * sigma^2));

psi = @(x) x.*exp(-x);
x1 = 0.0;
x2 = x1 + fzero(@(x) x.*exp(-x) - h, 2.5);

initial_profile = @(x) sign(x-x1).*psi(abs(x-x1)) + sign(x2-x).*psi(abs(x2-x));

%% Run Dynamics
[x, t, uHist] = finiteElementsCollocationMethod(h, external_input, initial_profile );

figure;
imagesc(t,x,uHist');
colorbar;
title('Temperature_plot');
xlabel('time_coordinates');
ylabel('x_coordinates');
axis xy;

```

## References

- [1] Shun-ichi Amari. Dynamics of pattern formation in lateral-inhibition type neural fields. *Biological Cybernetics*, 27(2):77–87, 1977.
- [2] Daniele Avitabile. Projection methods for neural field equations. *SIAM Journal on Numerical Analysis*, 61(2):562–591, 2023.
- [3] György Buzsáki and Andreas Draguhn. Oscillatory neural networks in the hippocampus and neocortex. *The European journal of neuroscience*, 20(11):2799–2812, 2004.
- [4] György Buzsáki and Andreas Draguhn. Propagating waves of activity in the neocortex: What they are, what they do. *Neuroscientist*, 10(5):371–378, 2004.
- [5] Andreas K Engel, Pascal Fries, and Wolf Singer. Dynamic predictions: oscillations and synchrony in top–down processing. *Nature Reviews Neuroscience*, 2(10):704–716, 2001.
- [6] Y. Fisher, Z. Lu, and R. Sperling. Ring attractor dynamics emerge from a spiking model of the entire protocerebral bridge. *Frontiers in Behavioral Neuroscience*, 13:63, 2019.
- [7] Richard FitzHugh. Impulses and physiological states in theoretical models of nerve membrane. *Biophysical journal*, 1(6):445, 1961.
- [8] David Golomb and Yosef Amitai. Neural dynamics in a model of the thalamocortical system. ii. the role of neural synchrony tested through perturbations of spike timing. *Cerebral Cortex*, 7(3):228–236, 1997.
- [9] Sung Soo Kim, Hervé Rouault, Shaul Druckmann, and Vivek Jayaraman. Ring attractor dynamics in the drosophila central brain. *Science*, 356(6340):849–853, 2017.
- [10] Ayelet N Landau and Pascal Fries. A neural mechanism for gamma/beta oscillation generation and its role in temporal attention. *Proceedings of the National Academy of Sciences*, 109(32):13490–13495, 2012.
- [11] Paul L Nunez and Ramesh Srinivasan. *Electric Fields of the Brain: The Neurophysics of EEG*. Oxford University Press, 2006.
- [12] Alfio Quarteroni and Fausto Saleri. *Scientific Computing with MATLAB and Octave*. Springer, 2 edition, 2006.

- [13] Grace M Richard and Thomas J O'Donnell. Bursting as a source of non-linear determinism in the firing patterns of nigral dopamine neurons. *Brain research*, 855(1):27–40, 2000.
- [14] Terrence J Sejnowski and Ole Paulsen. Traveling waves in visual perception. *Nature*, 439:85–92, 2006.
- [15] Haim Sompolinsky, Andrea Crisanti, and Hans-Jürgen Sommers. Chaotic behavior in neural networks. *Physical Review Letters*, 61(3):259, 1988.
- [16] Hugh R Wilson and Jack D Cowan. Excitatory and inhibitory interactions in localized populations of model neurons. *Biophysical journal*, 12(1):1, 1972.